Cancer Therapy: Preclinical

Clinical Cancer Research

^{131}I-labeled Anti-HER2 Camelid sdAb as a Theranostic Tool in Cancer Treatment

Matthias D'Huyvetter[1], Jens De Vos[1,2], Catarina Xavier[1], Marek Pruszynski[3], Yann G.J. Sterckx[4], Sam Massa[4,5], Geert Raes[4,5], Vicky Caveliers[1,6], Michael R. Zalutsky[7], Tony Lahoutte[1,6], and Nick Devoogdt[1]

Abstract

Purpose: Camelid single-domain antibody-fragments (sdAb) have beneficial pharmacokinetic properties, and those targeted to HER2 can be used for imaging of HER2-overexpressing cancer. Labeled with a therapeutic radionuclide, they may be used for HER2-targeted therapy. Here, we describe the generation of a ^{131}I-labeled sdAb as a theranostic drug to treat HER2-overexpressing cancer.

Experimental Design: Anti-HER2 sdAb 2Rs15d was labeled with ^{131}I using [^{131}I]SGMIB and evaluated *in vitro*. Biodistribution was evaluated in two HER2$^+$ murine xenograft models by micro-SPECT/CT imaging and at necropsy, and under challenge with trastuzumab and pertuzumab. The therapeutic potential of [^{131}I]SGMIB-2Rs15d was investigated in two HER2$^+$ tumor mouse models. A single-dose toxicity study was performed in mice using unlabeled [^{127}I]SGMIB-sdAb at 1.4 mg/kg. The structure of the 2Rs15d–HER2 complex was determined by X-ray crystallography.

Results: [^{131}I]SGMIB-2Rs15d bound specifically to HER2$^+$ cells ($K_d = 4.74 \pm 0.39$ nmol/L). High and specific tumor uptake was observed in both BT474/M1 and SKOV-3 tumor xenografted mice and surpassed kidney levels by 3 hours. Extremely low uptake values were observed in other normal tissues at all time points. The crystal structure revealed that 2Rs15d recognizes HER2 Domain 1, consistent with the lack of competition with trastuzumab and pertuzumab observed *in vivo*. [^{131}I]SGMIB-2Rs15d alone, or in combination with trastuzumab, extended median survival significantly. No toxicity was observed after injecting [^{127}I]SGMIB-2Rs15d.

Conclusions: These findings demonstrate the theranostic potential of [^{131}I]SGMIB-2Rs15d. An initial scan using low radioactive [*I]SGMIB-2Rs15d allows patient selection and dosimetry calculations for subsequent therapeutic [^{131}I]SGMIB-2Rs15d and could thereby impact therapy outcome on HER2$^+$ breast cancer patients. *Clin Cancer Res; 23(21); 6616–28. ©2017 AACR.*

Introduction

The HER2 is overexpressed in multiple human cancers including breast, ovarian, colorectal, and urothelial carcinomas (1). Its incidence in breast cancer is about 20%–30% and is often associated with a higher recurrence rate and a shorter time to relapse (2, 3). Upon breast cancer diagnosis, approximately 10% of women have metastatic disease, which is considered incurable. Treatment goals are mainly focused on prolonging overall survival (OS) and progression-free survival (PFS). Therapies targeting HER2 can significantly impact the outcome of HER2$^+$ metastatic breast cancer (4)—since the introduction of anti-HER2 drugs to the standard of care, OS has increased significantly. However, emerging resistance to trastuzumab and the kinase inhibitor lapatinib are frequently observed. Trastuzumab emtansine (T-DM1), an antibody–drug conjugate, combines the antitumor effects of trastuzumab with those of the microtubule-inhibitory agent DM1, a cytotoxic agent that is released within target cells. T-DM1 has shown therapeutic potential for the treatment of advanced breast cancer patients that progressed after combined treatment with trastuzumab and taxane (5). Unfortunately, most patients eventually progress on T-DM1 due to acquired resistance (6). Combining versatile HER2 therapies that can circumvent drug resistance are therefore of high importance (7).

Targeted radionuclide therapy (TRNT) deploys therapeutic radiolabeled molecules like mAbs, mAb fragments, peptides, or synthetic proteins that interact with tumor-associated membrane proteins, and targets both the primary tumor site as well as metastases. The integration of molecular imaging can assist to predict successful TRNT. This theranostic approach aims to include an identical imaging compound (8) to predict targeting and potential toxicity to healthy tissues. Currently, one mAb-based TRNT agent is commercially used, that is, the anti-CD20 mAb ^{90}Y-ibritumomab for treating B-cell non-Hodgkin lymphoma (9–11). Peptide receptor radionuclide therapy (PRRNT) shows efficacy in patients with neuroendocrine tumors (12) and is currently also being investigated in prostate and pancreatic carcinomas (12, 13).

Camelid single-domain antibody-fragments (sdAb), also referred to as VHHs or nanobodies, may solve some of the

[1]In Vivo Cellular and Molecular Imaging Laboratory, Vrije Universiteit Brussel, Brussels, Belgium. [2]Camel-IDS NV/SA, Brussels, Belgium. [3]Institute of Nuclear Chemistry and Technology, Warsaw, Poland. [4]Cellular and Molecular Immunology, Vrije Universiteit Brussel, Brussels, Belgium. [5]Myeloid Cell Immunology Laboratory, VIB-UGent Center for Inflammation Research, Gent, Belgium. [6]Nuclear Medicine Department, UZ Brussel, Brussels, Belgium. [7]Department of Radiology, Duke University Medical Center, Durham, North Carolina.

Note: Supplementary data for this article are available at Clinical Cancer Research Online (http://clincancerres.aacrjournals.org/).

Corresponding Author: Matthias D'Huyvetter, In Vivo Cellular and Molecular Imaging Laboratory, Vrije Universiteit Brussel, Laarbeeklaan 103, 1090 Brussels, Belgium. Phone: 322-477-4991; Fax: 322-477-5017; E-mail: mdhuyvet@vub.ac.be

doi: 10.1158/1078-0432.CCR-17-0310

Translational Relevance

HER2 is an interesting therapeutic target because it is overexpressed in cancers including breast, ovarian, and gastric. There is a need for strategies to overcome resistance to HER2-targeted therapies for metastatic breast cancer. SdAbs are a promising platform for both imaging and targeted therapy. The ^{68}Ga-labeled HER2-targeting variant was successfully evaluated before in a first clinical study in breast cancer patients to noninvasively detect HER2 expression using PET. We describe here a novel [^{131}I]-labeled sdAb that allows imaging for patient selection and HER2-targeted radionuclide therapy using the same compound. By targeting domain I of HER2, [^{131}I]SGMIB-2Rs15d allows administration to patients who progress on trastuzumab, pertuzumab, or T-DM1. These results indicate that [^{131}I]SGMIB-2Rs15d, with its low toxicity profile and proven therapeutic efficacy, has strong potential as a theranostic drug for clinical translation. A first-in-human study evaluating [^{131}I]SGMIB-2Rs15d in healthy volunteers and HER2^{+} breast cancer patients is currently ongoing (NCT02683083).

issues related to the use of other targeting vehicles such as mAbs for theranostic application. SdAbs (10–15 kDa) are antigen-binding fragments that are derived from *Camelidae* heavy-chain antibodies and have advantageous characteristics compared with mAbs and their derived fragments for *in vivo* targeting (14). Because of their smaller size, high stability, and exceptionally specific targeting, sdAbs have become valuable theranostic drugs. SdAbs directed at a variety of membrane-bound cancer biomarkers such as CEA, EGFR, HER2, and PSMA have been successfully evaluated as *in vivo* theranostic tracers using a variety of radionuclides in preclinical studies (8, 15–17). We recently reported a first-in-human PET study with ^{68}Ga-labeled anti-HER2 sdAb 2Rs15d for breast cancer imaging (18, 19). 2Rs15d was initially selected because of its noncompeting character with trastuzumab and pertuzumab for HER2-binding (20) and could therefore have its use as a therapeutic in tumors resistant to these agents. To this, 2Rs15d was previously applied as a vehicle for preclinical TRNT after labeling with ^{177}Lu (21). Crucial for the success of future therapeutic sdAb-based applications are reducing kidney retention of radiolabeled sdAbs, which could otherwise lead to renal toxicity. Indeed, substantial retention of radioactivity in kidneys is observed after intravenous injection of radiometal–sdAb conjugates (8, 17, 21), leading us to shift our focus to the use of radiohalogens for labeling sdAbs.

Herein, we describe the generation of a theranostic anti-HER2 sdAb using the radiohalogen ^{131}I [$t_{1/2} = 8.02$ d, $\langle E_\beta(\text{mean})\rangle = 190$ keV, $\langle E\gamma\rangle = 364$ keV]. 2Rs15d was radiolabeled with ^{131}I via the residualizing prosthetic group *N*-succinimidyl 4-guanodinomethyl-3-[*I]benzoate ([*I]SGMIB) (22). The reason for selecting [*I]SGMIB was twofold: (i) this prosthetic group was designed to have rapidly clearing catabolites, which should help reduce kidney dose from small radiolabeled biomolecules that are filtered via kidneys (23); (ii) the high pKa of its guanidino group interferes with the transport of labeled catabolites out of lysosomes, thereby trapping the radioiodine in cancer cells (24). The improved tumor targeting of a [*I]SGMIB-labeled anti-HER2 sdAb was first shown with 5F7GGC sdAb (25). Unfortunately, 5F7GGC competes with trastuzumab for binding to domain IV on HER2 (25), thereby compromising its clinical translation and not offering solutions to certain HER2 treatment resistance mechanisms (7). The goal of this study was to generate a potentially more clinically relevant theranostic drug by labeling the anti-HER2 sdAb 2Rs15d with [^{131}I]SGMIB.

Materials and Methods

General

All reagents were purchased from Sigma-Aldrich except when noted. Sodium [^{131}I]iodide in 0.1 N NaOH with a specific activity >185 GBq/mg was purchased from Perkin-Elmer. All reagents used in cell culture experiments were purchased from Gibco BRL except when noted. SdAbs were generated as described previously (18). HER2-targeting 2Rs15d, HER2-targeting but trastuzumab-competing 2Rb17c, and nontargeting R3B23 (control sdAb) were fully characterized previously (18, 20, 26). Trastuzumab (Herceptin) and pertuzumab (Perjeta, Hoffmann-La Roche Ltd) were used as stated in the experiments.

Determination of the HER2–2Rs15d complex crystal structure

Protein purification, crystallization of the HER2–2Rs15d complex, and structural determination were performed by PROTEROS. Detailed methods for crystallization, data collection, and structure determination are given in the Supplementary Materials and Methods and are summarized in Supplementary Table S1. The crystallographic data for the HER2–2Rs15d complex have been deposited in PDB (ID 5MY6).

Preparation of [^{131}I]-labeled compounds

[^{131}I]SGMIB was synthesized and purified as reported previously (25), and summarized in Supplementary Materials and Methods. Quality control (QC) was performed by instant thin-layer chromatography (iTLC) using glass microfiber sheets impregnated silica gel strips (Agilent) run with PBS, pH = 7.4. In parallel, radio-size exclusion chromatography (SEC, 0.5 mL/minute, 0.02 mol/L phosphate buffer, and 0.28 mol/L NaCl, pH = 7.4, Superdex 75 5/150 GL, 5 bar) was performed. [^{131}I]-2Rs15d was incubated in PBS at 25°C. Aliquots were obtained up to 144 hours and analyzed with radio-HPLC using a polystyrene divinylbenzene copolymer column (PLRP-S 30Å, 5 mm, 250/4 mm; Agilent) with the following gradient: (A: 0.1% trifluoroacetic acid in water; B: acetonitrile): 0–5 minutes, 25% B; 5–7 minutes, 25%–34% B; 7–10 minutes, 75%–100% B; and 10–25 minutes, 100% B, at a flow rate of 1 mL/minute. [^{131}I]-2Rs15d was also incubated in human serum at 37°C for 1 week and analyzed by radio-SEC. [*I]SGMIB-sdAbs are further referred to as [*I]-sdAbs.

Cell culture conditions

The HER2^{+} BT474/M1 breast cancer cell line was selected for its increased tumorigenicity (27), while HER2^{+} JIMT-1 for its resistance toward trastuzumab (28). Both cell lines were cultured in DMEM medium. The HER2^{+} SKOV-3 and the HER2^{+}/luciferase^{+} SKOV-3.IP1 (29) ovarian cancer cell lines (ATCC) were cultured using McCoy 5A medium. All media were enriched with 10% FBS, and a mixture of 100 U/mL penicillin and 0.1 mg/mL streptomycin (Invitrogen). Cells were grown in a humidified atmosphere with 5% CO_2 at 37°C. Prior to use for *in vitro* and *in vivo* purposes, cells were detached using trypsin-EDTA. HER2 expression of the different cell lines was confirmed by flow cytometry (Supplementary Materials and Methods). Tumor cell lines all overexpressed HER2, with ΔMFIs of 7135, 3592, and 2430 for BT474/M1, SKOV-3, and JIMT-1, respectively.

Targeting specificity, affinity, and cell-internalizing properties of [*I]-2Rs15d

HER2-binding kinetics of 2Rs15d and unlabeled [^{127}I]-2Rs15d and their noncompeting character with trastuzumab and pertuzumab was assessed via surface plasmon resonance (SPR) as described previously (18). Binding of control sdAb, 2Rs15d, 2Rb17c, and trastuzumab on BT474/M1 and JIMT-1 cells was evaluated using flow cytometry (Supplementary Materials and Methods). The binding characteristics of [^{131}I]-2Rs15d were evaluated on SKOV-3 and BT474/M1 cells. A total of 8×10^4 cells were adhered overnight and washed two times with PBS prior to addition of radioiodinated sdAbs. Binding specificity was measured by incubating cells with 20 nmol/L of [^{131}I]-2Rs15d and [^{131}I]-control sdAb, and challenged with a 100-fold molar excess of 2Rs15d, trastuzumab, or pertuzumab. Binding of [^{131}I]-2Rs15d, [^{131}I]-2Rb17c, and [^{131}I]-trastuzumab to JIMT-1 cells was assessed in parallel. Binding affinity was determined by incubating the plated cells with serial dilutions of [^{131}I]-2Rs15d, ranging from 0 to 300 nmol/L. A 100-fold molar excess of 2Rs15d was added in parallel to measure the degree of nonspecific binding. Cells were incubated for 1 hour at 4°C, after which unbound activity was washed away. Finally, cells were lysed by addition of 1 mol/L NaOH, and collected.

Intracellular retention of [^{131}I]-2Rs15d was evaluated at different time points on BT474/M1 cells. A total of 8×10^5 cells were adhered overnight and washed 2 times with PBS prior to incubation with 25 nmol/L of [^{131}I]-2Rs15d at 4°C for 1 hour. A 100-fold molar excess of unlabeled 2Rs15d was added in parallel to assess nonspecific binding. Next, the unbound fraction was washed away and cells were supplemented with fresh medium and incubated at 37°C for 24 hours. After incubation, supernatants were collected (dissociated fraction) prior to an acid wash of the cells using 0.05 mol/L glycine-HCl pH = 2.8, to collect the membrane-bound fraction. Cells were lysed with 1 mol/L NaOH to determine the internalized fraction. All fractions were counted for radioactivity using an automated gamma counter.

Animal models

Normal male C57Bl/6 mice were used to assess blood clearance. Toxicity analysis was performed in normal male and female Swiss albino mice. Female CRL:Nu-FoxN1nu mice were implanted with a 60-day slow-release estrogen pellet, after which they were inoculated in the right hind leg with 1×10^7 BT474/M1 cells in 1/1 Matrigel/cell culture medium. Tumors were grown to 284 ± 171 mm^3 for imaging and dissections, and to 50 ± 30 mm^3 for therapy. The same strain was also inoculated with 4×10^6 SKOV-3 cells in cell culture medium and grown until they reached 450 ± 100 mm^3 for imaging, and intraperitoneally (i.p.) inoculated with 0.5×10^6 SKOV-3.IP1 cells in case of therapy (29). Tumor growth was measured using caliper or bioluminescence imaging after intraperitoneal injection of 150 mg/kg Luciferin (30). All animal protocols were approved by the ethical committee of the Vrije Universiteit Brussel (14-272-5).

Biodistribution of [^{131}I]-2Rs15d via molecular imaging

BT474/M1 and SKOV-3 tumor xenografted mice were intravenously (i.v.) injected in the tail vein with 9.00 ± 0.18 MBq (4.0 μg; 0.32 nmol) [^{131}I]-2Rs15d ($n = 3$ per model), followed by micro-SPECT/CT imaging after 1, 4, and 24 hours. Mice were anaesthetized using 2% isoflurane and kept warm using a heating pad. Micro-SPECT/CT imaging was performed with a Vector$^+$/CT MILabs system, using a PET-collimator and a spiral scan mode of 94 bed positions (19s per position). For CT, a normal scan mode of only one position was used. The obtained SPECT data were reconstructed with a 0.6 voxel size, 2 subsets, and 7 iterations, after which images were fused and corrected for attenuation based on the CT scan. Images were analyzed using a medical image data analysis tool (AMIDE) and OsiriX. Uptake of [^{131}I]-2Rs15d in organs and tissues was analyzed and expressed as % injected activity per cubic centimeter (%IA)/cc.

Blood clearance of [^{131}I]-2Rs15d

Normal C57Bl/6 mice were injected intravenously with either 2.55 ± 0.81 MBq (4.0 μg; 0.32 nmol) [^{131}I]-2Rs15d or 1.75 ± 0.04 MBq (4.0 μg; 0.29 nmol) [^{131}I]-control sdAb ($n = 6$). Blood samples were collected regularly with a microcapillary until 180 min postinjection. Results were expressed as %IA per total blood volume (%IA/TBV), estimated as 7% of the total body weight. The blood half-life was determined through a biphasic nonlinear regression fit.

Biodistribution of [^{131}I]-2Rs15d via serial dissections

Groups of mice with BT474/M1 xenografts ($n = 3$) were injected intravenously with 0.97 ± 0.34 MBq (2.0 μg; 0.16 nmol) [^{131}I]-2Rs15d or with 1.02 ± 0.05 MBq (2.0 μg; 0.15 nmol) [^{131}I]-control. Mice were euthanized at several time points up to 120 hours, dissected, and major organs and tissues were isolated, weighed, counted, and expressed as %IA per gram of tissue (%IA/g). Urine samples were collected and analyzed using radio-SEC. In parallel, [^{131}I]-2Rs15d was administered to mice that were treated 72 hours prior with a 100-fold molar excess of trastuzumab, pertuzumab (2.4 mg, 16 nmol), or both combined ($n = 4$). Statistical analyses were performed using one-way ANOVA.

Organ-absorbed doses of [^{131}I]-2Rs15d

The biodistribution data were time-integrated to obtain the residence time per gram tissue (21, 25). Briefly, the area under the curve between 0 and 120 hours was made using the trapezoid integration method. Next, the absorbed doses were calculated using S values for ^{131}I obtained from RADAR phantoms (Unit Density Spheres). The S value for a 1 g sphere (0.0304 Gy.g/MBq.s) was used to calculate all organ doses. In parallel, an estimation of organ-absorbed doses was performed by extrapolation to the adult female phantom with OLINDA 1.0 software using a voiding bladder interval of 1 hour. The calculations were based on time–activity curves to determine the number of disintegrations in organs. Organ doses and effective dose were calculated using the appropriate weighing factors.

Therapeutic efficacy of [^{131}I]-2Rs15d

In the first experiment, BT474/M1 tumor xenografted mice ($n = 6$) received 5 intravenously injections (weekly, for 5 weeks) of either [^{131}I]-2Rs15d (10.83 ± 1.73 MBq; 8.0 μg;

0.63 nmol/treatment), [^{131}I]-control sdAb (8.8 ± 2.9 MBq; 8.0 μg; 0.57 nmol/treatment), or vehicle solution. In the second experiment, SKOV-3.IP1 tumor xenografted mice ($n = 8$) were injected with 5 intravenous doses (weekly, for 5 weeks) of either (i) 8.8 ± 1.4 MBq [^{131}I]-2Rs15d (8.0 μg; 0.63 nmol/treatment), (ii) trastuzumab at 7.5 mg/kg loading (190 μg; 1.3 nmol); 3.5 mg/kg maintenance (90 μg; 0.6 nmol) + 5.5 ± 2.4 MBq [^{131}I]-2Rs15d (8.0 μg; 0.63 nmol/treatment), (iii) unlabeled 2Rs15d at 7.5 mg/kg loading (190 μg; 15 nmol); 3.5 mg/kg maintenance (90 μg; 7 nmol), (iv) trastuzumab regimen alone, or (v) an equal volume of vehicle solution. Tumor volume (via caliper or bioluminescence imaging) and animal weight were measured weekly. Dropouts were considered when one of the following endpoints was reached: for subcutaneous tumors (i) tumor size of >1,000 mm^3, (ii) >20% weight loss, or (iii) the presence of necrotic tumor tissue; for intraperitoneal tumors (i) exceeding a BLI signal of 5.0×10^7 ph/s/cm^2/sr, (ii) severe ascites, or (iii) a sudden >20% weight loss. Survival curves were plotted and analyzed by the log-rank Mantel–Cox test.

Toxicity of [^{127}I]-2Rs15d

A single dose (1.4 mg/kg) of nonradioactive [^{127}I]-2Rs15d formulation was administered intravenously to 30 mice. The dose level of 1.4 mg/kg is 1,000 times the expected dose in human as required by the microdosing toxicity guideline of EMEA (CPMP/ICH/286/95), currently used in the first-in-human clinical study in which a single injection of low radioactive [^{131}I]SGMIB-2Rs15d (<100 μg) is administered. The concurrent control group received vehicle solution only. Parameters evaluated were clinical signs, mortality, changes in body weight and food intake, hematology and clinical chemistry parameters, organ weights, and gross pathology. The mice were sacrificed on day 2 (10 mice/sex/group) and on day 15 (remaining 5 mice/sex/group).

Results

Determination of the HER2–2Rs15d complex crystal structure

The crystal structure of the HER2–2Rs15d complex reveals that the sdAb interacts with an epitope located on HER2 domain I. This is distinct from the HER2 sites recognized by trastuzumab and pertuzumab (Fig. 1A) and most other reported HER2 binders (Supplementary Fig. S1A and S1B).

As expected, interactions with HER2 are mediated by 2Rs15d residues located in the complementarity determining regions (CDR); however, an almost equal number of amino acids located in the framework regions (FR) also contribute to HER2 recognition. Importantly, none of the 2Rs15d residues involved in HER2 binding are lysines (Supplementary Fig. S1C), the site of SGMIB conjugation. A detailed description of the interactions between 2Rs15d and HER2 domain I is presented in Supplementary Fig. S1D and Supplementary Table S2.

Preparation of [^{131}I]-labeled compounds

[^{131}I]SGMIB was synthesized ($n = 35$) from its tin precursor in 31.6% ± 6.6% radiochemical yield and 98.2% ± 1.2% purity after HPLC purification. The conjugation efficiency of [^{131}I]SGMIB to biomolecules was 36.5% ± 12.8% ($n = 25$) for [^{131}I]-2Rs15d, 36.1% ± 10.0% ($n = 7$) for [^{131}I]-control sdAb, 44.2% ± 0.2% ($n = 2$) for [^{131}I]-2Rb17c and 57.5% ± 2.1% ($n = 2$) for [^{131}I]-trastuzumab with a specific activity ranging from 0.06 to 2.55 MBq/μg. Radiochemical purity was >97% for all prepared compounds.

The stability of [^{131}I]-2Rs15d was analyzed in PBS at 25°C and in serum at 37°C via radio-HPLC and SEC. [^{131}I]-2Rs15d was stable in PBS, with >95% intact conjugate up to 72 hours, decreasing to 93% at 144 hours (Fig. 2A). In human serum, 95% of [^{131}I]-2Rs15d was still intact after 24 hours, gradually decreasing to 87% at 168 hours.

Targeting specificity, affinity, and cellular internalization of [*I]-2Rs15d

Besides binding to recombinant HER2 protein, 2Rs15d and [*I]-2Rs15d were also tested on cancer cells with various levels of functional HER2 expression, namely trastuzumab-sensitive BT474/M1 and SKOV-3 cells, and trastuzumab-resistant JIMT-1 cells (in which HER2 domain IV is obscured by overexpressed MUC4; ref. 28).

Binding affinities to HER2 of 3.99 ± 0.04 nmol/L and 3.62 ± 0.03 nmol/L for 2Rs15d and [^{127}I]-2Rs15d, were determined by SPR (Fig. 2B and C). [^{131}I]-2Rs15d bound specifically on BT474/M1 cells, while [^{131}I]-control sdAb exhibited negligible HER2 binding (Fig. 2D). The noncompeting character of unlabeled 2Rs15d with trastuzumab and pertuzumab was confirmed via SPR measurements (Fig. 1B and C), and [^{131}I]-2Rs15d on BT474/M1 and SKOV-3 cells (Fig. 1D and E). [^{131}I]-2Rs15d bound about 1.5 and 4 times better to JIMT-1 cells compared with HER2-domain IV–specific compounds [^{131}I]-2Rb17c sdAb and [^{131}I]-trastuzumab respectively, while binding to BT474/M1 was similar for all three (Fig. 1F and G). These observations were confirmed by flow cytometry (Fig. 1H). The binding affinity of [^{131}I]-2Rs15d, measured by incubating BT474/M1 cells with serial dilutions of [^{131}I]-2Rs15d, indicated a K_d = 4.74 ± 0.39 nmol/L (Fig. 2E). The cell-associated fraction of [^{131}I]-2Rs15d remained stable over time, ranging between 20%–30% of initially bound activity (Fig. 2F). At 1 hour, 17.00% ± 0.69% was membrane-bound and 9.13% ± 2.37% was internalized. At 24 hours, 28.79% ± 1.95% of [^{131}I]-2Rs15d remained cell associated of which about half was internalized and half bound to membrane.

Blood clearance and biodistribution of [^{131}I]-2Rs15d

Consecutive micro-SPECT/CT images in BT474/M1 (Fig. 3A) and SK-OV-3 (Fig. 3B) subcutaneous tumor xenografted mice were generated and quantified (Fig. 3C; Supplementary Table S3) after intravenous injection of [^{131}I]-2Rs15d. In the BT474/M1 model, high contrast images were obtained as early as 1 hour postinjection, with most [^{131}I]-2Rs15d concentrated in kidneys (20.75% ± 4.18% IA/cc) and tumor (6.48% ± 2.58% IA/cc). The accumulation in kidneys dropped significantly to 4.54% ± 0.81% IA/cc after 4 hours, and to a value below 0.5% IA/cc after 24 hours, while the fraction in tumor remained 4.54% ± 0.81% IA/cc after 4 hours and 2.50% ± 1.22% IA/cc after 24 hours. Very low uptake values were measured for thyroid and muscle. Similar results were obtained with the SKOV-3 model, although lower tumor uptake was measured (2.31% ± 0.22% IA/cc after 1 hour and 1.16% ± 0.03% IA/cc after 24 hour), due to the lower HER2 expression compared with BT474/M1.

[^{131}I]-2Rs15d was cleared from blood in a biphasic manner (Fig. 4A). The calculated half-lives for the initial fast blood pool vanishing phase were about 1.93 ± 0.13 minutes for

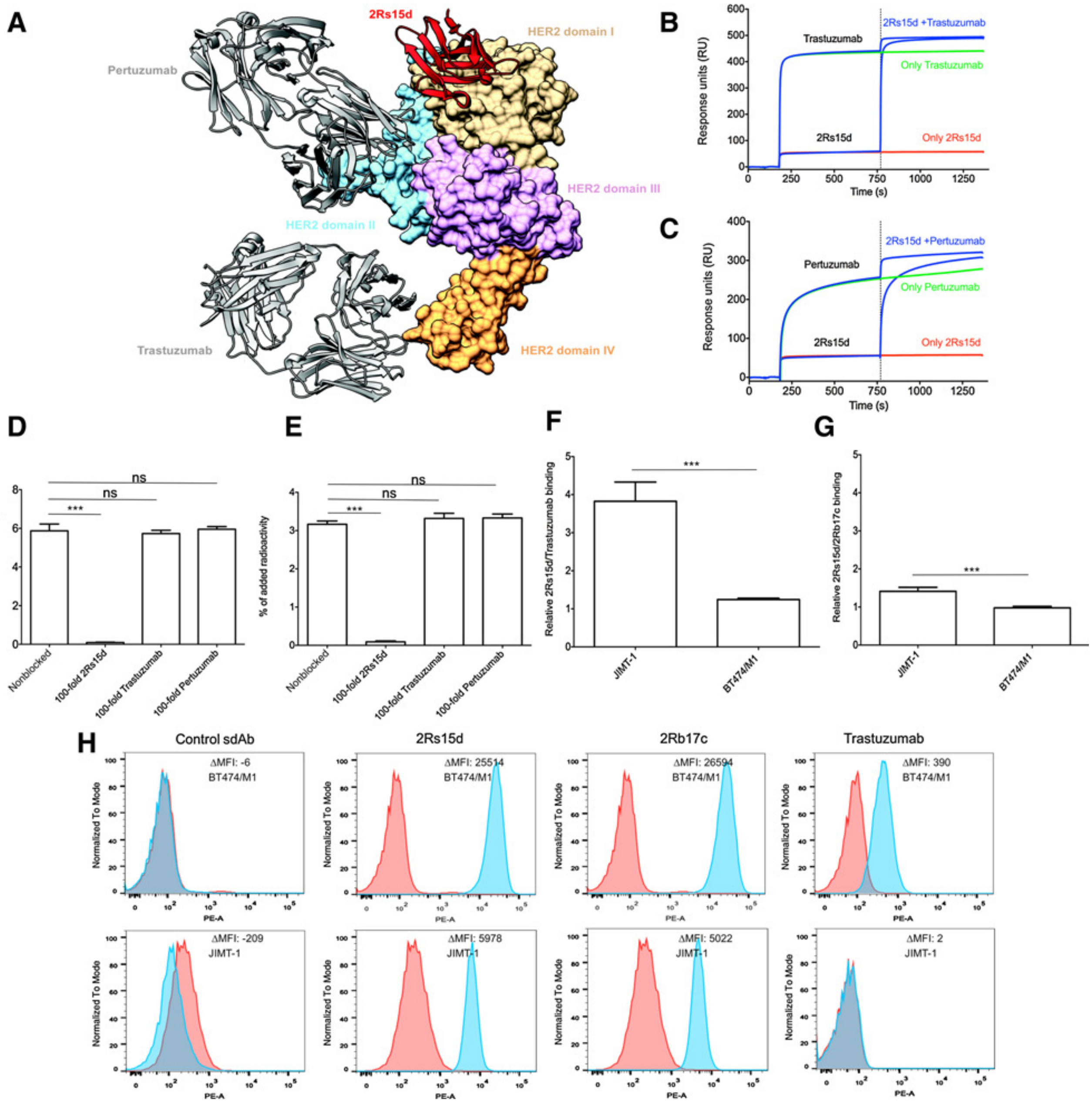

Figure 1.

A, Structure of 2Rs15d (cartoon representation) complexed with HER2(1-646)His (surface representation). 2Rs15d (red) binds HER2 domain I (tan; Gln2-Arg196), while pertuzumab and trastuzumab interact with domain II (sky blue; Thr197–Val320) and domain IV (sandy brown; Cys490–Cys566), respectively. HER2 domain III (Cys321–Ala489) is colored in plum. **B** and **C,** Competition studies with [^{127}I]-2Rs15d and anti-HER2 mAbs trastuzumab and pertuzumab for binding to HER2. **B,** Binding of [^{127}I]-2Rs15d and/or trastuzumab and **C,** [^{127}I]-2Rs15d and/or pertuzumab to immobilized HER2-Fc protein. Competition between two components occurs when the signal obtained by binding of a mixture of the two is lower than the sum of the signals obtained by each component individually. **D** and **E,** [^{131}I]-2Rs15d does not compete for HER2 receptor binding with trastuzumab and pertuzumab on BT474/M1 (**D**) and SKOV-3 cells (**E**); its binding to HER2 could be blocked only by a 100-fold excess of unlabeled 2Rs15d, but not by a 100-fold excess of unlabeled trastuzumab or pertuzumab. ***, $P < 0.0001$; ns, not significant, using one-way ANOVA. **F** and **G,** Degree of HER2 targeting of [^{131}I]-2Rs15d compared with [^{131}I]-trastuzumab and [^{131}I]-2Rb17c on trastuzumab-resistant JIMT-1 and trastuzumab-responsive BT474/M1 cells. **F,** [^{131}I]-2Rs15d binds about 4 times higher to JIMT-1 cells compared with [^{131}I]-trastuzumab, while binding to BT474/M1 was similar for both. **G,** Binding to JIMT-1 was only 1.5 times higher for [^{131}I]-2Rs15d compared with [^{131}I]-2Rb17c. ***, $P < 0.0001$ using Student t test. **H,** Control sdAb does not bind to HER2 on BT474/M1 and JIMT-1 cells, as determined by flow cytometry (described in Supplementary Materials and Methods). HER2-targeting sdAbs 2Rs15d and 2Rb17c bind to HER2 on both cell lines, while trastuzumab binds HER2 on BT474/M1 cells but not on JIMT-1 cells.

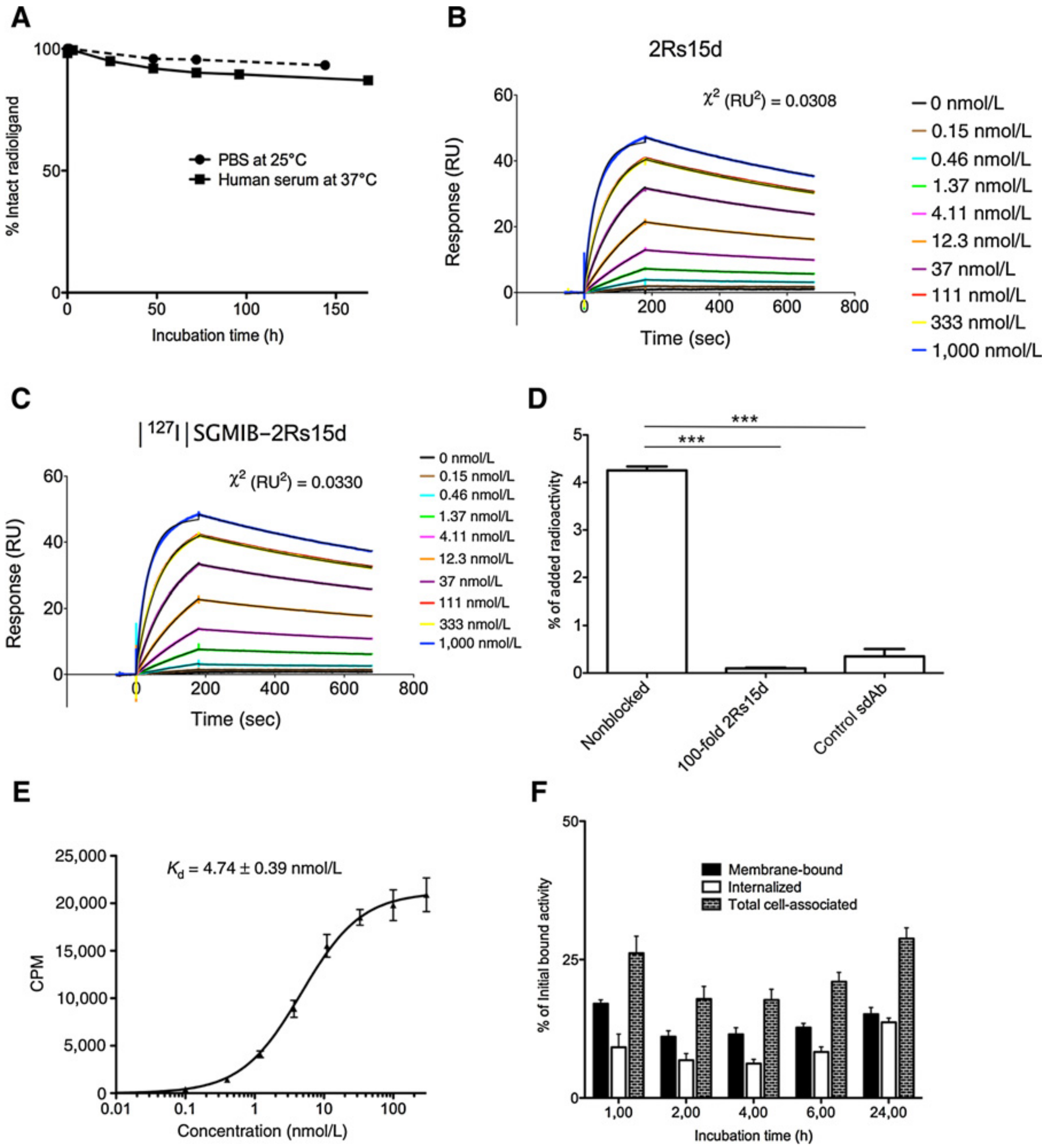

Figure 2.

A, [^{131}I]-2Rs15d is stable in PBS at 25°C up to 144 hours, and in human serum at 37°C up to 168 hours. More than 95% of the activity was found in the protein fraction after 72-hour incubation in PBS, and about 95% after 24-hour incubation in human serum. **B** and **C,** SPR measurements revealed HER2 binding affinities of $K_d = 3.99 \pm 0.04$ nmol/L (K_a (1/Ms): 2.21E+5; K_d (1/s): 8.79E-4) for 2Rs15d (**B**) and 3.62 ± 0.03 nmol/L (K_a (1/Ms): 2.35E+5; K_d (1/s): 8.53E-4) for [^{127}I]-2Rs15d (**C**). **D,** [^{131}I]-2Rs15d binds specifically to HER2; its binding to HER2 could be blocked by a 100-fold excess of unlabeled 2Rs15d. Binding of [^{131}I]-control sdAb to HER2 was negligible. Data are presented as mean ± SD ($n = 3$). ***, $P < 0.0001$ using one-way ANOVA. **E,** Saturation binding assay resulted in a calculated affinity of K_d of 4.74 ± 0.39 nmol/L for [^{131}I]-2Rs15d on BT474/M1 cells. Data are presented as mean ± SD ($n = 3$). **F,** Internalization of [^{131}I]-2Rs15d into BT474/M1 cells. The different cellular fractions of [^{131}I]-2Rs15d are shown for up to 24 hours of incubation at 37°C. Data are presented as mean ± SD ($n = 3$) and expressed as % of initial bound activity at time points 1, 2, 4, 6, and 24 hours.

[^{131}I]-2Rs15d and 1.87 ± 0.13 minutes for [^{131}I]-control sdAb. After 60 minutes, less than 2% IA/TBV was measured in blood for both sdAbs. No significant difference ($P = 0.66$) was observed.

A summary of the biodistribution data of [^{131}I]-2Rs15d and [^{131}I]-control sdAb in BT474/M1 tumor xenografted mice is presented in Fig. 4B and Supplementary Table S4. The highest tumor uptake for [^{131}I]-2Rs15d was observed after 1 hour, with

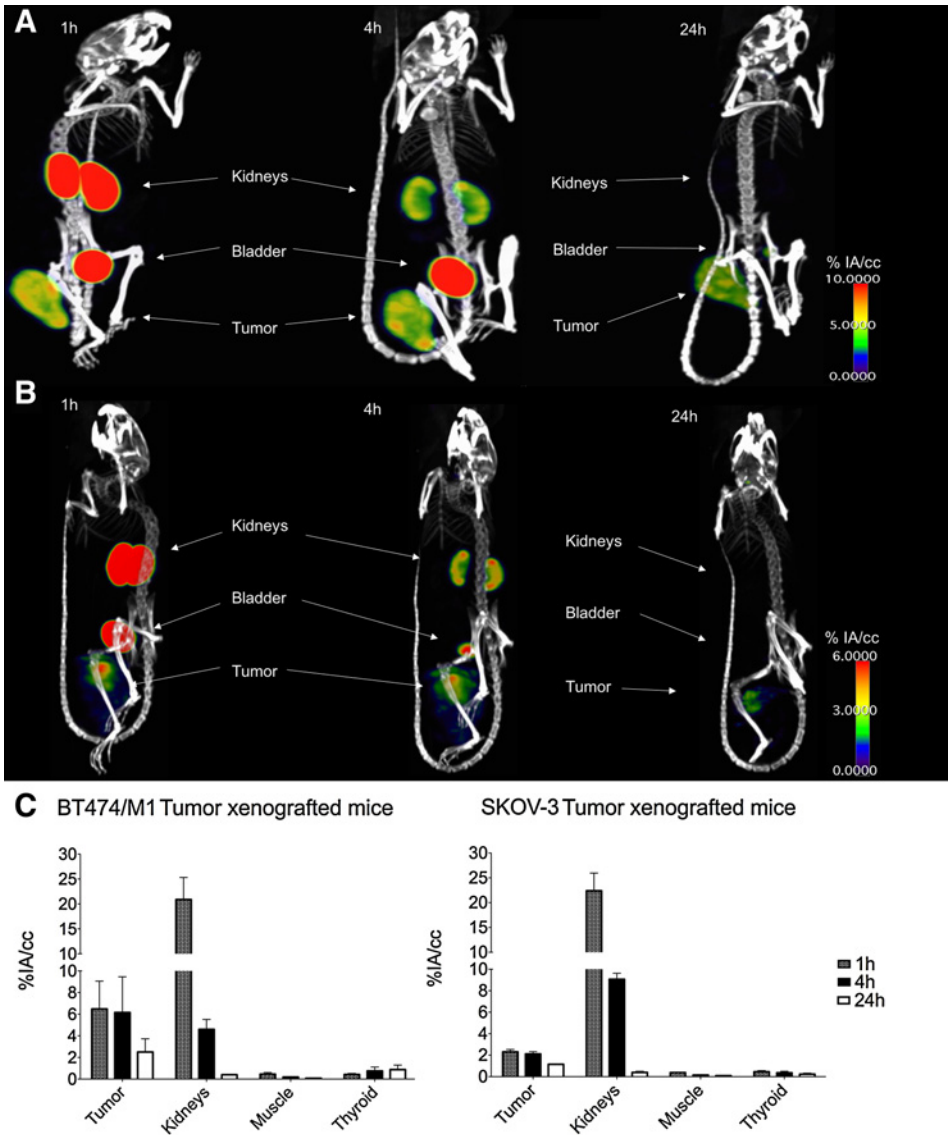

Figure 3.
Micro-SPECT/CT images obtained in HER2^{+} tumor models BT474/M1 (**A**) and SKOV-3 (**B**), 1, 4, and 24 hours after injection of [^{131}I]-2Rs15d. Accumulation of radioactivity was observed in kidneys, bladder, and tumor, indicated by white arrows. **C,** *In vivo* (% IA/cc) quantification of tracer uptake after 1, 4, and 24 hours in BT474/M1 and SKOV-3 xenografted mice. Data are presented as mean ± SD ($n = 3$).

a value of 20.22% ± 1.64% IA/g, while only 0.14% ± 0.06% IA/g was observed in tumor after 4 hours for [^{131}I]-control sdAb. Tumor retention of [^{131}I]-2Rs15d decreased to 5.10% ± 1.90% IA/g at 24 hours and to 0.40% ± 0.05% IA/g at 72 hours. In kidneys, 55.63% ± 8.47% IA/g was measured for [^{131}I]-2Rs15d at 1 hour, decreasing rapidly to 0.94% ± 0.52% IA/g at 24 hours and to 0.24% ± 0.14% IA/g at 72 hours. Thyroid uptake was very low at all time points, indicating no substantial dehalogenation occurred. Radioactivity concentration in the other tissues was low. Radio-SEC indicated that about 80% of the radioactivity was present in urine as intact [^{131}I]-2Rs15d at 30 minutes, decreasing to 15% and 4% at 1 and 3 hours, confirming that [^{131}I]-SGMIB labeling generates rapidly excreted labeled catabolites (21). No significant differences (P = 0.617) in tumor targeting were observed between animals receiving [^{131}I]-2Rs15d alone (11.00% ± 3.94% IA/g) and animals pretreated with trastuzumab (9.31% ± 2.35% IA/g), pertuzumab (8.91% ± 2.06% IA/g), or both (8.59% ± 2.85% IA/g), as presented in Fig. 4C and Supplementary Table S5. Likewise, no differences in normal tissue uptake between the groups was observed.

[^{131}I]-2Rs15d organ-absorbed doses

Organ-absorbed doses from 37 MBq of [^{131}I]-2Rs15d are summarized in Supplementary Table S4. The highest absorbed dose was delivered to tumor (11.88 Gy), while kidneys received 8.36 Gy. Doses delivered to other healthy organs and tissues were very low. The absorbed doses calculated for cumulative administration of 46.25 MBq [^{131}I]-2Rs15d and 27.75 MBq of [^{131}I]-2Rs15d + trastuzumab for therapy (see below) are depicted in Fig. 5A. Patient organ-absorbed doses were estimated using OLINDA via extrapolation to the adult female phantom (Table 1). The effective dose for the adult female was 0.0273 mSv/MBq.

Therapeutic efficacy of [^{131}I]-2Rs15d

BT474/M1 xenografted mice receiving [^{131}I]-2Rs15d had a significant longer ($P < 0.05$) median survival of 137.5 days versus

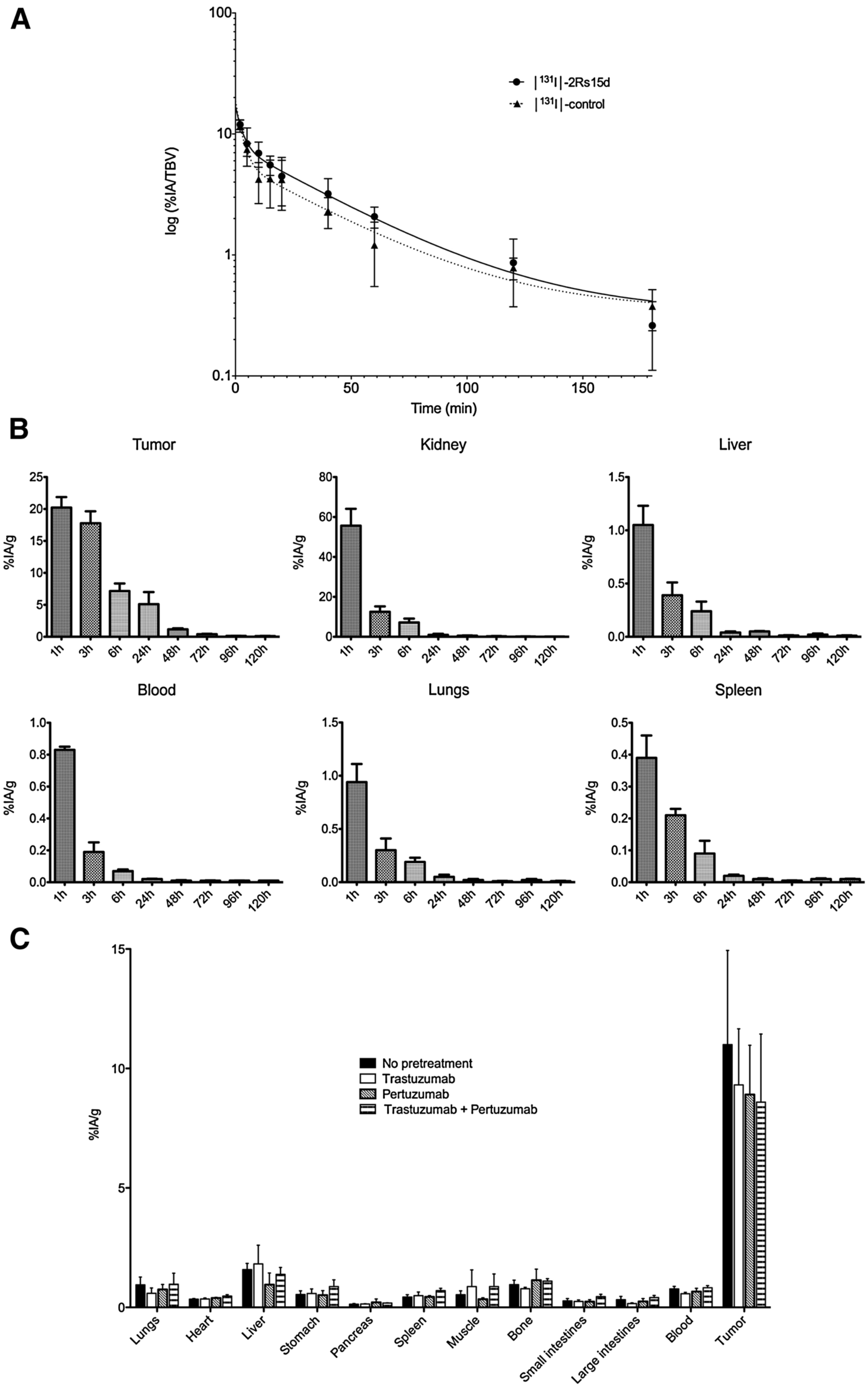

Figure 4.

A, Semi-log plot of blood clearance data for [^{131}I]-2Rs15d and [^{131}I]-control sdAb in normal mice ($n = 6$). Data are presented as % IA per total blood volume (% IA/TBV). **B,** Tumor and tissue distribution of [^{131}I]-2Rs15d in mice with BT474/M1 xenografts up to 120 hours postinjection. Data are presented as mean ± SD ($n = 3$). **C,** *Ex vivo* biodistribution of [^{131}I]-2Rs15d after 1 hour in BT474/M1 tumor xenografted mice pretreated 72 hours earlier with a 100-fold molar excess of trastuzumab, pertuzumab, or both. ($n = 4$). Values (mean ± SD) are expressed as % IA/g, except for thyroid for which % IA was used. No significant differences in tumor targeting were observed ($P = 0.617$), determined with one-way ANOVA.

93.5 and 78 days for mice receiving [^{131}I]-control sdAb and vehicle, respectively (Fig. 5B and C). No statistically significant difference in survival was observed between control groups ($P = 0.98$). Moreover, half of the animals receiving [^{131}I]-2Rs15d showed absence of tumors after 150 days, compared with only 1 of 6 in the vehicle group and 0 of 6 in the [^{131}I]-control sdAb group.

In the second experiment performed in an aggressive trastuzumab-responsive metastatic model, SKOV-3.IP1 xenografted mice treated with [^{131}I]-2Rs15d had a significantly longer

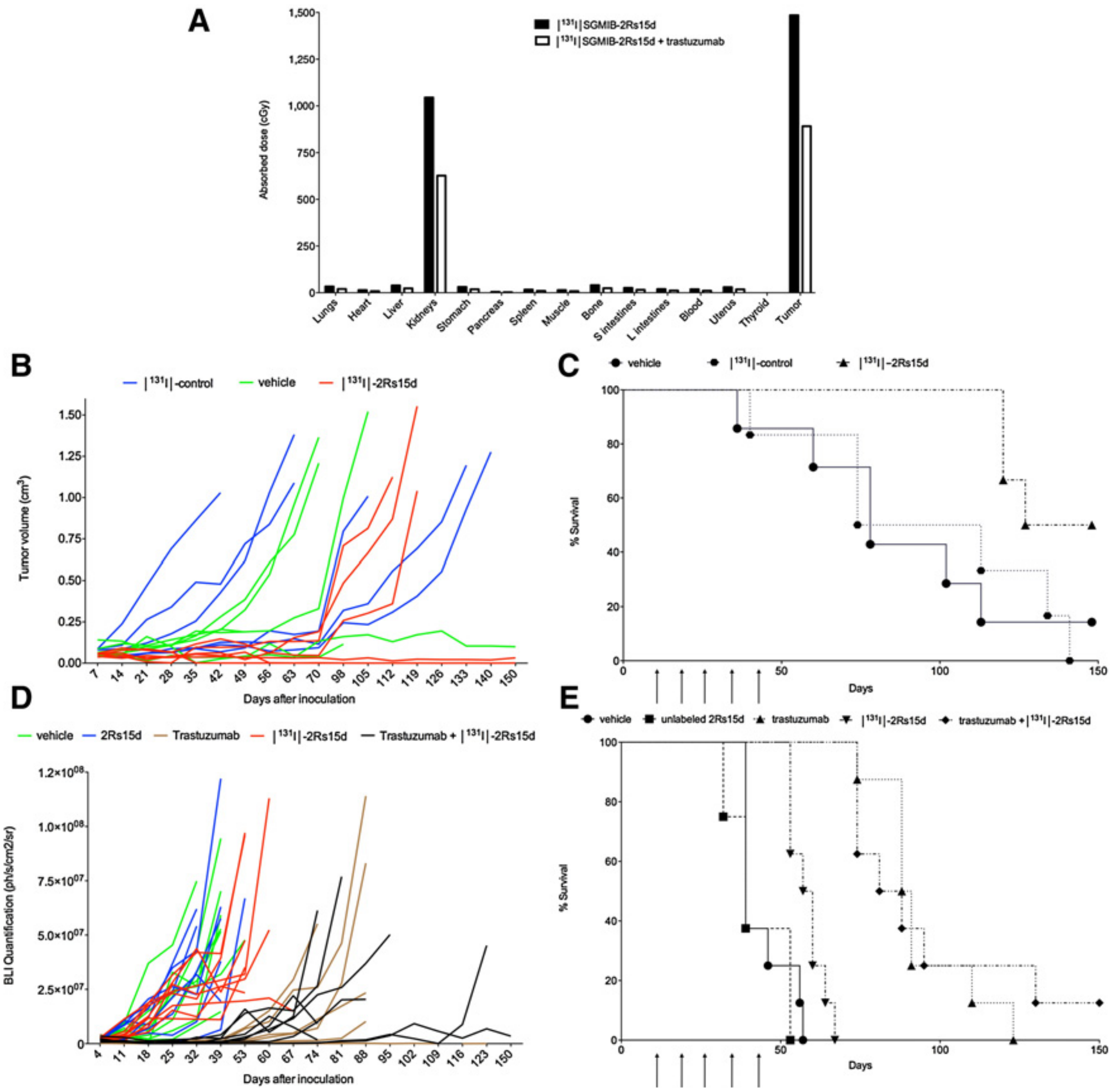

Figure 5.

A, Calculated absorbed doses to normal organs and tumor for a cumulative administration of 46.25 MBq [^{131}I]-2Rs15d and trastuzumab + 27.75 MBq of [^{131}I]-2Rs15d, the doses used in the therapy experiments presented in **B**, **C** and **D**, **E**. **B,** Tumor volumes (mm^3) for individual mice in function of time during therapy. Mice were euthanized when tumor size exceeded 1,000 mm^3, a sudden >20% weight loss was measured, or when necrotic tumor tissue presented. **C,** Survival after treatment with [^{131}I]-2Rs15d or [^{131}I]-control sdAb in mice with BT474/M1 xenografts ($n = 6$). Mice injected with [^{131}I]-control sdAb reached tumors >1,000 mm^3 between 40 and 140 days, which led to a median survival of 93 days. In the group injected with vehicle solution, three animals reached tumors >1,000 mm^3 between 78 and 113 days. Two animals developed necrotic tumors and were euthanized after 36 and 102 days. After 150 days, one animal in the vehicle group had a small lesion of about 110 mm^3. Three animals treated with [^{131}I]-2Rs15d developed tumors exceeding 1,000 mm^3 between 120 and 127 days after tumor cell inoculation. The other three animals were tumor-free after 150 days. Survival was significantly longer for animals in the treated group compared with those in the control groups ($P < 0.05$), as determined with log-rank Mantel–Cox test. Moreover, half of the animals receiving [^{131}I]-2Rs15d showed complete absence of tumors after 150 days. **D,** BLI quantification of tumor tissue in the peritoneum for individual mice in function of time during therapy. Mice were euthanized when the quantified BLI signal exceeded 5.0 × 10^7 ph/s/cm^2/sr, when severe ascites was observed or when a sudden >20% weight loss was measured. **E,** Therapeutic efficacy of [^{131}I]-2Rs15d, trastuzumab or a combination of both in mice with SKOV-3.IP1 xenografts ($n = 8$). All animals reached a BLI signal in peritoneum of 5.0 × 10^7 ph/s/cm^2/sr, except for two animals in the trastuzumab group (day 112 and 126) and one in the trastuzumab + [^{131}I]-2Rs15d group (day 88) which were euthanized due to a >20% weight loss. One animal in the PBS (day 39), 2Rs15d (day 39), and trastuzumab (day 88) group, and three animals in the [^{131}I]-2Rs15d group (day 53 and 67) were euthanized due to severe ascites. One animal in the trastuzumab + [^{131}I]-2Rs15d was alive at the end of the study. No significant difference in survival was observed between the groups receiving vehicle and unlabeled 2Rs15d ($P = 0.37$). Mice treated with [^{131}I]-2Rs15d had a significantly longer median survival of 59 days, versus only 39 days for mice receiving unlabeled 2Rs15d or vehicle solution respectively ($P < 0.005$, log-rank Mantel–Cox test). Trastuzumab treatment led to a median survival of 89 days, while mice receiving [^{131}I]-2Rs15d + trastuzumab had a median survival of 85 days (difference not significant, $P = 0.84$, log-rank Mantel–Cox test). Median survival in both groups receiving trastuzumab was significantly longer than that for animals receiving [^{131}I]-2Rs15d alone ($P < 0.0001$, log-rank Mantel–Cox test).

Table 1. Radiation dose estimates of [^{131}I]-2Rs15d to different organs for adult female human based on OLINDA calculations

Target organ	Total (mSv/MBq)
Adrenals	2.17E−04
Brain	7.27E−07
Breasts	5.84E−05
Gallbladder wall	7.33E−04
Lower large intestine wall	7.99E−03
Small Intestine	3.17E−03
Stomach wall	3.52E−04
Upper large intestine wall	2.45E−03
Heart wall	7.12E−05
Kidneys	4.43E−04
Liver	2.62E−04
Lungs	6.49E−05
Muscle	1.83E−03
Ovaries	7.45E−03
Pancreas	2.66E−04
Red marrow	1.27E−03
Osteogenic cells	8.93E−04
Skin	6.16E−04
Spleen	2.63E−04
Thymus	3.93E−05
Thyroid	8.87E−06
Urinary bladder wall	4.91E−01
Uterus	1.58E−02
Total body	1.86E−03
Effective dose equivalent	3.33E−02
Effective dose	2.73E−02

NOTE: Data are presented as mSv/MBq. The effective dose for the adult female was 0.0273 mSv/MBq.

median survival, 59 days, versus 39 days for mice receiving unlabeled 2Rs15d or vehicle solution ($P < 0.005$; Fig. 5D and E). No significant difference in survival was observed between the groups receiving vehicle or unlabeled 2Rs15d ($P = 0.37$). Trastuzumab treatment led to a median survival of 89 days, while mice receiving [^{131}I]-2Rs15d + trastuzumab had a median survival of 85 days (difference not significant, $P = 0.84$). Median survival in both groups receiving trastuzumab was significantly longer than that for animals receiving [^{131}I]-2Rs15d alone ($P < 0.0001$).

Toxicity of [^{127}I]-2Rs15d

A single dose of 1.4 mg/kg [^{127}I]-2Rs15d caused no toxicity during the 15-day observation period. No mortality or clinical signs of toxicity, or change in body weight were observed in this preliminary study. No treatment-related changes in hematology, clinical chemistry, terminal fasting body weights, organ weights/ratios, and gross pathology were seen.

Discussion

About 20%–30% of breast cancers overexpress HER2, resulting in a more aggressive phenotype with a poor prognosis. HER2-directed therapies increase OS; however, a significant fraction of patients suffer from relapse and disease progression (4). Resistance to HER2-directed therapies occurs either through mechanisms at the HER2 target or through bypass signaling (7). Trastuzumab resistance can occur through mutations to its HER2 epitope or the presence of truncated and isoforms of HER2 like p95HER2 (31) and D16 HER2 (32). Moreover, coexpression of proteins like MUC1 and 4 can prevent trastuzumab from binding HER2 (28, 33). Mutations in the kinase domain of HER2 can lead to lapatinib resistance (34). The cytotoxic effect of T-DM1 is dependent on the intracellular concentration of DM-1. Consequently, mechanisms that lead to impaired HER2-binding or receptor-mediated endocytosis will influence therapeutic efficacy significantly (6). As more data emerge suggesting that combining versatile HER2-therapies can abolish drug resistance, novel strategies that target HER2 at multiple points become clinically important.

We generated a library of anti-HER2 sdAbs (20) from which 2Rs15d was selected as the lead compound based on its overall optimal properties including high affinity and *in vivo* tumor targeting, and for its noncompeting character with trastuzumab and pertuzumab for HER2 targeting. 2Rs15d was validated preclinically labeled with the diagnostic radionuclides ^{18}F (35), ^{68}Ga (18, 19) and ^{111}In (36). Labeled with ^{68}Ga, 2Rs15d was evaluated in a first clinical trial, where we showed that it was safe and accumulated preferentially in primary tumors and metastases of HER2^{+} breast cancer patients. Anti-drug antibody measurements from patient's blood revealed no preexisting or tracer-induced antibodies against 2Rs15d (19). In addition, we developed [^{177}Lu]DTPA-2Rs15d for TRNT in mice with HER2^{+} xenografts (21). Reduced renal retention was partially achieved by coinjection of 150 mg/kg Gelofusin. Fractionated treatment with [^{177}Lu]DTPA-2Rs15d in mice bearing subcutaneous SKOV-3 tumors led to almost complete tumor regression and significantly improved median survival. This was achieved with a cumulative absorbed dose of 40 Gy to tumor for 150 MBq [^{177}Lu]DTPA-2Rs15d, but also 40 Gy delivered to kidneys, thereby exceeding the threshold for renal toxicity (23 Gy). Histologic analyses after 150 days did not reveal any signs of nephrotoxicty (21); however radiation-induced damage to kidneys can occur later. For clinical translation, a further reduction of renal retention would be an important benefit.

The rationale for using [^{131}I]-2Rs15d in this study is threefold: (i) the theranostic character of *I allows SPECT (^{131}I, ^{123}I) and PET (^{124}I) imaging to calculate the dosimetry of the identical therapeutic counterpart; (ii) proof-of-concept studies have shown that labeling sdAbs with [^{131}I]SGMIB reduces tracer accumulation in kidneys significantly without compromising *in vivo* targeting and stability (25); and (iii) 2Rs15d does not compete with trastuzumab and pertuzumab, permitting the administration of [^{131}I]-2Rs15d to patients undergoing HER2-targeting therapies and more importantly to those that progress on trastuzumab and T-DM1. There are several possible mechanisms for trastuzumab resistance. When resistance occurs through HER2 downregulation or shedding of its extracellular domain, [^{131}I]-2Rs15d will not be able to bind either. In certain tumors, a fraction of HER2 molecules are proteolytically shed, resulting in for example truncated p95HER2 which is found in about 10%–30% of HER2-overexpressing tumors (31, 37). With the proposed technology, low radioactive dose [*I]-2Rs15d will allow the selection of patients who still have sufficient intact HER2 to be eligible for therapeutic [^{131}I]-2Rs15d. Also, as 2Rs15d binds HER2 domain I, which is most distant from the cell membrane, it might be less influenced by epitope masking agents, or by domain IV mutations that prevent trastuzumab and T-DM1 from binding HER2 (28, 31–33). As steric interference by MUC4 can play an important role in this process, we therefore focused on this mechanism. Recently, it was shown that TNFα can induce MUC4 expression in HER2-positive breast and gastric cancer cells (37). Moreover, they observed a strong association between MUC4-positive tumors and a shorter DFS in patients receiving adjuvant trastuzumab-based treatment (38). We show here that [^{131}I]-2Rs15d binds four times higher to JIMT-1 compared with [^{131}I]-trastuzumab, while binding to trastuzumab-responsive BT474/M1 was similar for both compounds (Fig. 1F and G). In contrast, the trastuzumab-competing sdAb 2Rb17c outperformed trastuzumab on the same cell line, which implies that a smaller-sized sdAb was less hindered by the presence of MUC4. In addition, as the cytotoxic β^--particles of ^{131}I transverse multiple cell diameters, the therapeutic effect of [^{131}I]-2Rs15d might be less influenced by impaired cell-internalization or intratumoral HER2 heterogeneity including the presence of truncated HER2 in a subfraction of tumor cells, compared with trastuzumab and T-DM1 (6).

We here showed that [^{131}I]-2Rs15d binds specifically to HER2, and when injected intravenously in mice, it is eliminated from blood rapidly. High contrast micro-SPECT/CT images delineated tumors as early as 1 hour postinjection in two distinct HER2$^+$ mouse models. The clearance of [^{131}I]-2Rs15d from kidneys was faster than ever observed for this sdAb (18, 20, 21, 35, 36). For example, dosimetric calculations revealed that 37 MBq of [^{131}I]-2Rs15d achieved an absorbed dose of only 8 Gy to kidneys. This is an important improvement compared with the absorbed doses recalculated for 37 MBq [^{177}Lu]DTPA-2Rs15d, in tandem with 150 mg/kg gelofusin treatment, to kidneys (10 Gy) (21). Analysis of the radioactivity present in urine revealed the increasing presence of radiolabeled metabolites, confirming that [^{131}I]SGMIB indeed gives rise to rapidly clearing catabolites after renal filtration (23). This is an important benefit compared to the previously used radiometal chemistry that led to retained radioactivity in kidneys (18, 19, 21).

The tumor uptake for [^{131}I]-2Rs15d was lower than that obtained with [*I]-5F7GGC sdAb. Here, absorbed doses of 45 and 30 Gy were delivered to BT474/M1 tumors from 37 MBq (in two independent experiments), and about 18 and 16 Gy to kidneys (25). The difference in tumor uptake between 2Rs15d and 5F7GGC might be attributable to the fact that they target different HER2 epitopes (25). Because [*I]SGMIB traps radioiodine intracellularly, this effect is more pronounced for highly internalizing sdAbs like 5F7GGC than for moderately internalizing sdAbs like 2Rs15d. The faster washout from tumor in case of [^{131}I]-2Rs15d agrees with our previously obtained results with 2Rs15d (21).

Mice with BT474/M1 xenografts treated with [^{131}I]-2Rs15d had a significantly longer median survival (137.5 days) compared with animals receiving [^{131}I]-control sdAb (93.5 days) and vehicle (78 days) with half of the animals receiving [^{131}I]-2Rs15d exhibiting no visible evidence of tumor after 150 days (Fig. 5B and C). In the SKOV-3.IP1 metastatic model, treatment with [^{131}I]-2Rs15d prolonged median survival with 20 days compared with controls. Animals receiving either trastuzumab alone or in combination with [^{131}I]-2Rs15d lived on average 50 days longer than the controls, and on average 30 days longer than those treated with [^{131}I]-2Rs15d alone. Even more so, 12.5% of mice that received the combination of trastuzumab and [^{131}I]-2Rs15d were alive at the end of the study, confirming that repeated coadministration of [^{131}I]-2Rs15d does not negatively affect therapeutic outcome (Fig. 5D and E). It is important to note that this trastuzumab-responsive SKOV-3.IP1 model is very aggressive and is defined by rapid disease progression (29). Mice were treated with an optimized trastuzumab treatment over 5 weeks and progressed after treatment termination. We anticipated therefore that [^{131}I]-2Rs15d would not outperform the trastuzumab regimen. The limited median survival of mice treated with trastuzumab-alone and the combination might be related to the presence of surviving tumor clones with absent/lower HER2 expression. Whether trastuzumab treatment downregulates HER2 is still unclear (39).

It is encouraging to see that 46.25 MBq of [^{131}I]-2Rs15d shows therapeutic efficacy in two HER2$^+$ animal models, with an estimated absorbed dose of 15 Gy to tumor and only 10 Gy to kidneys (Fig. 4A). We did not expect the occurrence of nephrotoxicity, as we are well below the renal toxicity threshold of 23 Gy. A similar radioactive dose to kidneys using ^{177}Lu-PSMA I&T did not induce any late renal toxicity (40). The therapeutic effect obtained with [^{131}I]-2Rs15d was less pronounced compared with that obtained with [^{177}Lu]DTPA-2Rs15d (21), but in the latter, we administered about 150 MBq resulting in a recalculated absorbed dose to tumor of 40 Gy, compared with 15 Gy (at 46.25 MBq) to tumor in this study. On the basis of dosimetry calculations, we could increase the cumulative activity administered by twofold, without the need for extra kidney-protective measures such as coinjection with gelofusin and/or positively charged amino acids, which could theoretically lead to a tumor absorbed dose of 30 Gy. Future long-term studies of renal toxicity will be required (40). In addition, therapeutic efficacy of [^{131}I]-2Rs15d will be further assessed in the trastuzumab-resistant JIMT-1 model, which is targetable by 2Rs15d but not by trastuzumab. With these goals in mind, we are currently upscaling the radiochemical process to obtain higher radioactive levels of [^{131}I]-2Rs15d.

α-Particle–emitting isotopes might achieve higher therapeutic absorbed doses to tumors compared with β^--particles. However, as their path length is shorter, the cell killing efficiency is more influenced by receptor heterogeneity (41). Consequently, α-particle therapy might be more suited in a micrometastatic setting. In line with antibody–drug conjugates, sdAbs have been successfully conjugated with cytotoxic payloads like DM1 or PE38-toxin, showing efficient tumor growth control without systemic toxicity (42–44). However, selecting highly internalizing sdAbs will be mandatory to induce significant cytotoxic effects. In addition, receptor heterogeneity might affect therapeutic outcome, which can be effectively addressed with a cytotoxic agent such as ^{131}I with a multicellular range of action.

To our knowledge, this is the first study to describe a theranostic radiolabeled sdAb suitable for clinical translation. [^{131}I]-2Rs15d was successfully applied as an imaging agent using micro-SPECT/CT, and as a therapeutic agent in two distinct HER2$^+$ mouse models. Taken together, these data indicate that [^{131}I]-2Rs15d shows promise as a theranostic drug with a low toxicity profile, significant therapeutic efficacy and of potential benefit for patients that progress on trastuzumab, pertuzumab, or T-DM1. We envision the imaging component as a pretreatment scan after the administration of low radioactive dose [*I]-2Rs15d. This allows patient selection and exact dosimetry calculations for therapeutic [^{131}I]-2Rs15d, which could impact therapeutic outcome and an understanding of both therapeutic response as well as any normal tissue toxicities that might arise. A first-in-human clinical study is currently ongoing evaluating low radioactive dose [^{131}I]-2Rs15d in healthy volunteers and HER2$^+$ breast cancer patients (NCT02683083).

Disclosure of Potential Conflicts of Interest

M. D'Huyvetter is an employee of Camel-IDS and holds ownership interest (including patents) in Nanobody Therapeutics. J. De Vos holds ownership interest (including patents) in sdAb Therapeutics. G. Raes is an employee of, holds ownership interest (including patents) in, and is a consultant/advisory board member for Camel-IDS. T. Lahoutte is an employee of Camel-IDS, holds ownership interest (including patents) in Nanobody Therapeutics, and is a consultant/advisory board member for IBA and IRE Belgium. N. Devoogdt is an employee of Camel-IDS and holds ownership interest (including patents) in Camelid Single Domain Therapeutics. No potential conflicts of interest were disclosed by the other authors.

Authors' Contributions

Conception and design: M. D'Huyvetter, C. Xavier, T. Lahoutte, N. Devoogdt
Development of methodology: M. D'Huyvetter, C. Xavier, M. Pruszynski, M. Zalutsky, T. Lahoutte
Acquisition of data (provided animals, acquired and managed patients, provided facilities, etc.): M. D'Huyvetter, J. De Vos, C. Xavier, T. Lahoutte, S. Massa, N. Devoogdt
Analysis and interpretation of data (e.g., statistical analysis, biostatistics, computational analysis): M. D'Huyvetter, J. De Vos, C. Xavier, Y.G.J. Sterckx, S. Massa, G. Raes, T. Lahoutte, N. Devoogdt
Writing, review, and/or revision of the manuscript: M. D'Huyvetter, J. De Vos, C. Xavier, M. Pruszynski, Y.G.J. Sterckx, G. Raes, V. Caveliers, M. Zalutsky, N. Devoogdt
Administrative, technical, or material support (i.e., reporting or organizing data, constructing databases): M. D'Huyvetter, J. De Vos, Y.G.J. Sterckx
Study supervision: V. Caveliers, T. Lahoutte, N. Devoogdt

Acknowledgments

The authors thank Cindy Peleman, Jan De Jonge, and Claudia Mebis for technical assistance, Professor Marc Bracke of Ghent University for donating the SKOV-3.IP1 cell line, and Dr. Zéna Wimana (Bordet Institute, Brussels) for the JIMT-1 cell line.

Grant Support

This work was supported by Innoviris.Brussels (to N. Devoogdt and T. Lahoutte), Stichting Tegen Kanker (to C. Xavier and V. Caveliers), and in part by the National Cancer Institute Grant CA42324 (M. Zalutsky). M. D'Huyvetter is a postdoctoral fellow of the Research Foundation-Flanders, Belgium (FWO) and was supported by the Belgian American Education Foundation (BAEF) and the Germaine Eisendrath-Dubois Foundation. T. Lahoutte is a senior clinical investigator of the Research Foundation-Flanders, Belgium (FWO).

The costs of publication of this article were defrayed in part by the payment of page charges. This article must therefore be hereby marked *advertisement* in accordance with 18 U.S.C. Section 1734 solely to indicate this fact.

Received February 1, 2017; revised May 23, 2017; accepted July 21, 2017; published OnlineFirst July 27, 2017.

References

1. Hicks DG, Kulkarni S. HER2 breast cancer: review of biologic relevance and optimal use of diagnostic tools. Am J Clin Pathol 2008;129:263–27.
2. Tandon AK, Clark GM, Chamness GC, Ullrich A, McGuire WL. HER-2/neu oncogene protein and prognosis in breast cancer. J Clin Oncol 1989;7:1120–8.
3. Slamon DJ, Clark GM, Wong SG, Levin WJ, Ullrich A, McGuire WL. Human breast cancer: correlation of relapse and survival with amplification of the HER-2:neu oncogene. Science 1987;235:177–82.
4. Mendes D, Alves C, Alfonso N, Cardoso F, Passos-Coelho JL, Costa L, et al. The benefit of HER2-targeted therapies on overall survival of patients with metastatic HER2-positive breast cancer-a systematic review. Breast Cancer Res 2015;17:140.
5. Verma S, Miles D, Gianni L, Krop IE, Welslau M, Baselga J, et al. Trastuzumab emtansine for HER2-positive advanced breast cancer. N Engl J Med 2012;367:1783–91.
6. Barok M, Joensuu H, Isola J. Trastuzumab emtansine: mechanisms of action and drug resistance. Breast Cancer Res 2014;16:209.
7. Rexer BN, Artega CL. Intrinsic and acquired resistance to HER2-targeted therapies in HER2 gene-amplified breast cancer: mechanisms and clinical implications. Crit Rev Oncog 2012;17:1–16.
8. D'Huyvetter M, Xavier C, Caveliers V, Lahoutte T, Muyldermans S, Devoogdt N. Radiolabeled nanobodies as theranostic tools in targeted radionuclide therapy of cancer. Expert Opin Drug Deliv 2014;11:1939–54.
9. Martinez A, Martinez-Ramirez M, Martinez-Caballero D, Beneit P, Clavel J, Figueroa G, et al. Radioimmunotherapy for non-Hodgkin's lymphoma; positioning, safety, and efficacy of 90Y-Ibritumomab. 10 years of experience and follow-up. Rev Esp Med Nucl Imagen Mol 2017;36:13–19.
10. Larson SM, Carrasquillo JA, Cheung NK, Press OW. Radioimmunotherapy of human tumours. Nat Rev Cancer 2015;15:347–60.
11. Thurber GM, Schmidt MM, Wittrup KD. Antibody tumor penetration. Adv Drug Deliv Rev 2008;60:1421–34.
12. Zaknun JJ, Bodei L, Mueller-Brand J, Pavel ME, Baum RP, Hörsch D, et al. The joint IAEA, EANM, and SNMMI practical guidance on peptide receptor radionuclide therapy (PRRNT) in neuroendocrine tumours. Eur J Nucl Med Mol Imaging 2013;40:800–16.
13. Lütje S, Heskamp S, Cornelissen AS, Poeppel TD, van den Broek SAMW, Rosenbaum-Krumme S, et al. PSMA ligands for radionuclide imaging and therapy of prostate cancer: clinical status. Theranostics 2015;5:1388–401.
14. Hamers-Casterman C, Atarhouch T, Muyldermans S. Naturally occurring antibodies devoid of light chains. Nature 1993;363:446–48.
15. Chakravarty R, Goel S, Cai W. Nanobody: the "Magic Bullet" for molecular imaging? Theranostics 2014;4:386–98.
16. Vaneycken I, D'huyvetter M, Hernot S, De Vos J, Xavier C, Devoogdt N, et al. Immuno-imaging using nanobodies. Curr Opin Biotechnol 2011;22:877–81.
17. De Vos J, Devoogdt N, Lahoutte T, Muyldermans S. Camelid single-domain antibody-fragment engineering for (pre)clinical in vivo molecular imaging applications: adjusting the bullet to its target. Expert Opin Biol Ther 2013;13:1149–60.
18. Xavier C, Vaneycken I, D'huyvetter M, Heemskerk J, Keyaerts M, Vincke C, et al. Synthesis, preclinical validation, dosimetry and toxicity of ^{68}Ga-NOTA-Anti-HER2 nanobodies for immuno-PET imaging of HER2 receptor expression in cancer. J Nucl Med 2013;54:776–84.
19. Keyaerts M, Xavier C, Heemskerk J, Devoogdt N, Everaert H, Ackaert C, et al. Phase I study of 68Ga-HER2-nanobody for PET/CT assessment of HER2 expression in breast carcinoma. J Nucl Med 2016;57:27–33.
20. Vaneycken I, Devoogdt N, Van Gassen N, Vincke C, Xavier C, Wernery U, et al. Preclinical screening of anti-HER2 nanobodies for molecular imaging of breast cancer. FASEB J 2011;25:2433–2446.
21. D'Huyvetter M, Vincke C, Xavier C, Aerts A, Impens N, Baatout S, et al. Targeted radionuclide therapy with a ^{177}Lu-labeled anti-HER2 nanobody. Theranostics 2014;4:708–20.
22. Vaidyanathan G, Zalutsky MR. Synthesis of N-succinimidyl 4-guanidinomethyl-3-[*I]iodobenzoate: a radio-iodination agent for labeling internalizing proteins and peptides. Nat Protoc 2007;2:282–6.
23. Shankar S, Vaidyanathan G, Kuan C, Bigner DD, Zalutsky MR. Antiepidermal growth factor variant III scFv fragment: effect of radioiodination method on tumor targeting and normal tissue clearance. Nucl Med Biol 2006;33:101–10.
24. Vaidyanathan G, Jestin E, Olafsen T, Wu AM, Zalutsky MR. Evaluation of an anti-p185(HER2) (scFv-C(H)2-C(H)3)2 fragment following radioiodination using two different residualizing labels: SGMIB and IB-Mal-D-GEEEK. Nucl Med Biol 2009;36:671–80.
25. Pruszynski M, Koumarianou E, Vaidyanathan G, Revets H, Devoogdt N, Lahoutte T, et al. Improved tumor targeting of anti-HER2 nanobody through N-succinimidyl 4-guanidinomethyl-3-iodobenzoate radiolabeling. J Nucl Med 2014;55:650–6.
26. Lemaire M, D'Huyvetter M, Lahoutte T, Van Valckenborgh E, Menu E, De Bruyne E, et al. Imaging and radioimmunotherapy of multiple myeloma with anti-idiotypic nanobodies. Leukemia 2014;28:444–7.

27. Yu Z, Xia W, Wang HY, Wang SC, Pan Y, Kwong KY, et al. Antitumor activity of an Ets protein, PEA3, in breast cancer cell lines MDA-MB-361DYT2 and BT474M1. Mol Carcinog 2006;45:667–75.
28. Nagy P, Friedländer E, Tanner M, Kapanen AI, Carraway KL, Isola J, et al. Decreased accessibility and lack of activation of ErbB2 in JIMT-1, a Herceptin-resistance, MUC4-expressing breast cancer cell line. Cancer Res 2005;65:473–82.
29. De Vlieghere E, Carlier C, Ceelen W, Bracke M, De Wever O. Data on in vivo selection of SK-OV-3 Luc ovarian cancer cells and intraperitoneal tumor formation with low inoculation numbers. Data Brief 2016;6: 542–9.
30. Keyaerts M, Verschueren J, Bos TJ, Tchouate-Cainkam LO, Peleman C, Breckpot K, et al. Dynamic bioluminescence imaging for quantitative tumour burden assessment using IV or IP administration of D: -luciferin: effect on intensity, time kinetics and repeatability of photon emission. Eur J Nucl Med Mol Imaging 2008;35:999–1007.
31. Scaltriti M, Rojo F, Ocaña A, Anido J, Guzman M, Cortes J, et al. Expression of p95HER2, a truncated form of the HER2 receptor, and response to anti-HER2 therapies in breast cancer. J Natl Cancer Inst 2007;99:628–38.
32. Castiglioni F, Tagliabue E, Campiglio M, Pupa SM, Balsari A, Ménard S. Role of exon-16-deleted HER2 in breast carcinomas. Endocr Relat Cancer 2006;13:221–32.
33. Fessler SP, Wotkowicz MT, Mahanta SK, Bamdad C. MUC1* is a determinant of trastuzumab (Herceptin) resistance in breast cancer cells. Breast Cancer Res Treat 2009;118:113–24.
34. Wang SE, Narasanna A, Perez-Torres M, Xiang B, Wu FY, Yang S, et al. HER2 kinase domain mutation results in constitutive phosforylation and activation of HER2 and EGFR and resistance to EGFR tyrosine kinase inhibitors. Cancer Cell 2006;10:25–38.
35. Xavier C, Blykers A, Vaneycken I, D'Huyvetter M, Heemskerk J, Lahoutte T, et al. (18)F-nanobody for PET imaging of HER2 overexpressing tumors. Nucl Med Biol 2016;43:247–52.
36. Massa S, Xavier C, De Vos J, Caveliers V, Lahoutte T, Muyldermans S, et al. Site-specific labeling of cysteine-tagged cameld single-domain antibody-fragments for use in molecular imaging. Bioconjug Chem 2014;25:979–88.
37. Sáez R, Molina MA, Ramsey EE, Rojo F, Keenan EJ, Albanell J, et al. p95HER-2 predicts worse outcome in patients with HER-2-positive breast cancer. Clin Cancer Res 2006;12:424–31.
38. Mercogliano MF, Martino MD, Venturutti L, Rivas MA, Proietti CJ, Inurrigarro G, et al. TNFα-induced mucin 4 expression elicits trastuzumab resistance in HER2-positive breast cancer. Clin Cancer Res 2016;23: 636–48.
39. Nahta R, Yu D, Hung MC, Hortobagyi GN, Esteva FJ. Mechanisms of disease: understanding resistance to HER2-targeted therapy in human breast cancer. Nat Clin Pract Oncol 2006;3:269–80.
40. Chatalic KLS, Heskamp S, Konijnenberg M, Molkenboer-Kuenen JD, Franssen GM, Clahsen-van Groningen MC, et al. Towards personalized treatment of prostate cancer: PSMA I&T, a promising prostate-specific membrane antigen-targeted theranostic agent. Theranostics 2016;6: 849–61.
41. Akabani G, Carlin S, Welsh P, Zalutsky MR. In vitro cytotoxicity of 211At-labeled trastuzumab in human breast cancer cell lines: effect of specific activity and HER2 receptor heterogeneity on survival fraction. Nucl Med Biol 2006;33:333–47.
42. Fang T, Duarte JN, Ling J, Li Z, Guzman JS, Ploegh HL. Structurally-defined antiMHC-II nanobody-drug conjugates: therapeutic and imaging platforms for B-cell lymphoma. Angew Chem Int Ed Engl 2016;55:2416–20.
43. Tang J, Li J, Zhu X, Yu Y, Chen D, Yuan L, et al. Novel CD7-specific nanobody-based immunotoxins potently enhanced apoptosis of CD7-positive malignant cells. Oncotarget 2016;7:34070–83.
44. Yu Y, Li J, Zhu X, Tang X, Bao Y, Sun X, et al. Humanized CD7 nanobody-based immunotoxins exhibit promising anti-T-cell acute lymphoblastic leukemia potential. Int J Nanomedicine 2017;12:1969–83.